Dissociative recombination of N_2^+: An *ab initio* study

D. A. Little,[1] K. Chakrabarti,[2,3] J. Zs. Mezei,[2,4,5] I. F. Schneider,[2,4] and J. Tennyson[1]

[1]*Department of Physics and Astronomy, University College London, Gower Street, London, WC1E 6BT, United Kingdom*

[2]*LOMC CNRS-UMR-6294, Université du Havre, 76058 Le Havre, France*

[3]*Department of Mathematics, Scottish Church College, 1 & 3 Urquhart Sq., Kolkata 700 006, India*

[4]*Laboratoire Aimé-Cotton, CNRS/Université Paris Sud, Bat. 505, f-91405, Orsay, France*

[5]*Institute for Nuclear Research, Hungarian Academy of Sciences, P.O. Box 51, H-4001 Debrecen, Hungary*

(Received 6 September 2014; published 10 November 2014)

Cross sections for the dissociative recombination of N_2^+ for $v_i^+ = 0$–3 are computed using multichannel quantum defect theory with molecular data generated using the R-matrix method. The calculation is completely *ab initio* and includes three electronic cores of the ion. Extensive comparisons are made with previous experimental and theoretical studies. Our cross section is in excellent agreement with experimental results and other theoretical results. Cross sections and isotropic rate coefficients are provided for all computed vibrational levels.

DOI: 10.1103/PhysRevA.90.052705 PACS number(s): 34.80.Gs, 34.80.Ht, 34.80.Lx

I. INTRODUCTION

Molecular nitrogen is the most abundant molecule in the terrestrial atmosphere as well as in those of Titan and Triton. Its cation, N_2^+, is therefore prevalent in the earth's ionosphere as well as in nitrogen plasmas produced for reasons varying from lightning strikes to combustion. Unsurprisingly, there is a strong interest in characterizing nitrogen and there have been a number of recent attempts to put together comprehensive nitrogen chemistries for studies of plasmas containing molecular nitrogen [1–4].

Dissociative recombination (DR)

$$N_2^+ + e \rightarrow N_2^{**} \rightarrow N + N \tag{1}$$

is a vital process in these plasmas [5] as it is a major destroyer of N_2^+ ions. However, for reasons described below, the rate of DR, and other properties of the reaction, are poorly determined experimentally.

Storage rings have revolutionized our ability to measure DR rates reliably for small molecules [5,6], not least because the ability to store ions for a sufficiently long time for them to cool means that measurements can be made from vibrationally and rotationally cold molecules. It transpires, however, that N_2^+, which has no permanent dipole moment, is particularly difficult to cool even in long-lived beams in storage rings [7], and is also observed to be vibrationally hot in merged-beam experiments [8]. This means that the only available temperature-dependent N_2^+ DR rate measurements have been performed on vibrationally hot molecules [7–10]. Flowing afterglow Langmuir probe measurements have been made at 300 K [11–13]. Given this situation there is a clear need for vibrationally resolved theoretical studies, which can help provide reliable energy-dependent DR cross sections as function of vibrational state.

Guberman [14–18] has performed a series of calculations on the DR of N_2^+ using high-quality curves and couplings computed using standard quantum chemistry procedures and a multichannel quantum defect theory (MQDT) treatment of the actual DR process. Recently, two of us obtained comprehensive bound [19] and resonance [20] curves *ab initio* using the R-matrix method [21]. Previous studies using R-matrix curves for DR calculations [22–24] have obtained excellent results. However, for NO^+, a system with one less electron than N_2^+ and closed-shell core, it was found necessary to adjust the curves using experimental data in order to obtain reliable results [23]. Our aim here is for a completely *ab initio* treatment of the problem, where all parameters needed for the computation of a DR cross section are self-consistently calculated using the R-matrix method.

The paper is organized as follows: first we describe how we prepared the data from the R-matrix calculation for its use in an MQDT calculation, second a theoretical exposition of the cross-section calculation using MQDT is given with details of including core-excited bound Rydberg states, third a brief summary of computational details, and then our results with a discussion followed by our conclusions.

II. MOLECULAR DATA

The following minimal set of parameters are needed for an MQDT calculation of the DR cross section: the potential-energy curves (PEC) of the ground state of the ion, the PECs of the neutral molecule providing routes to dissociation (valence dissociative states), the electronic couplings between these neutral valence states (dissociative channels), and the Rydberg series converging to the ground state of the ion (ionization channels). For a MQDT calculation which includes "core-excited" initial states of the ion we additionally require the following: the PECs of the excited ion states, the electronic coupling between the valence states and the Rydberg series converging to each excited state of the ion, and the Rydberg-Rydberg coupling between each series converging to each state of ion.

A. Potential-energy curves

The data to form the potential-energy curves are taken from an R-matrix study using the UKRmol code suite [25], henceforth referred to as I [19] and II [20], respectively. The R-matrix method is a sophisticated quantum mechanical scattering technique and can be used to calculate bound and resonant (quasibound) electronic states of a molecule. For ionic targets the R-matrix method matches asymptotically to Coulomb functions; further details of the method can be found

in the review by one of us [21]. Bound states were calculated by solving for negative scattering energies using the module BOUND [19,25,26] and resonant states we found using the time-delay method with an improved fitting technique for overlapping resonances [20,27,28]. The calculations of the bound and resonant states are described extensively in I and II, respectively. By combining the data above (resonant) and below (bound) the ionization threshold of N_2^+, we have a complete description of the superexcited neutral electronic states which are important for dissociative recombination. The states which cross the ion ground state at favorable positions can then be identified. In the following discussion the N_2^+ states $X\ ^2\Sigma_g^+$, $A\ ^2\Pi_u$, and $B\ ^2\Sigma_g^+$ will be referred to as X, A, and B, respectively.

To form smooth potential-energy curves from the data presented in I and II it was necessary to fit the data with smoothing splines. The reasons for this were twofold. First, the R-matrix method works in the Born-Oppenheimer approximation and hence avoided crossings are present in the PECs. These avoided crossings were interpolated across using the smoothing spline; no formal diabatization took place. Secondly, for reasons described in detail in I and II, gaps in the data appear slightly above and slightly below the PEC of each electronic state of the ion. Therefore, it was necessary to interpolate across these gaps. An example of a smoothing spline being fitted to the adiabatic curves is given in Fig. 1.

To compute DR cross sections, it is necessary to know the asymptotic behavior of the PECs. The bound curves were extended using the R-matrix method in what will be termed "quantum chemistry (QC) mode." QC mode is an option that is available in UKRmol suite in which the spatial restriction of the R-matrix sphere is removed allowing the target plus scattering electron continuum orbitals to span an extended region. It was shown in I that, at points where there was little or no interaction with Rydberg states, the full scattering bound-state calculation and the QC-mode calculation gave almost identical results. The advantage of using the QC mode to extend the calculation to longer bond lengths is that it relies only on the diagonalization of a Hamiltonian [29] to find energy eigenvalues. This is more numerically stable than propagating and solving the R matrix, and it does not suffer from problems with the target wave function leaking outside the R-matrix sphere at large internuclear separations. Therefore, when one is only interested in low-lying bound states at long bond lengths, where there is no influence of Rydberg states, QC mode is the preferred option. Despite this, issues do arise when performing QC mode calculations at large internuclear separations. The number of target states used in an R-matrix calculation is arbitrary and their energetic order switches with internuclear separation leading to discontinuities in the calculated potential-energy curves, as is described in detail in I and II. Secondly, the continuum orbitals which are placed at the center of mass of the molecule become less appropriate at longer bond lengths. As we are only interested in the asymptote the state converges upon and the asymptotic behavior is easily predictable, these issues do not present significant problems.

The potential-energy curves taken from the data given in I and II with their asymptotes can be seen in Fig. 2 and Fig. 3. The smoothed curves are available in the Supplemental Material [44].

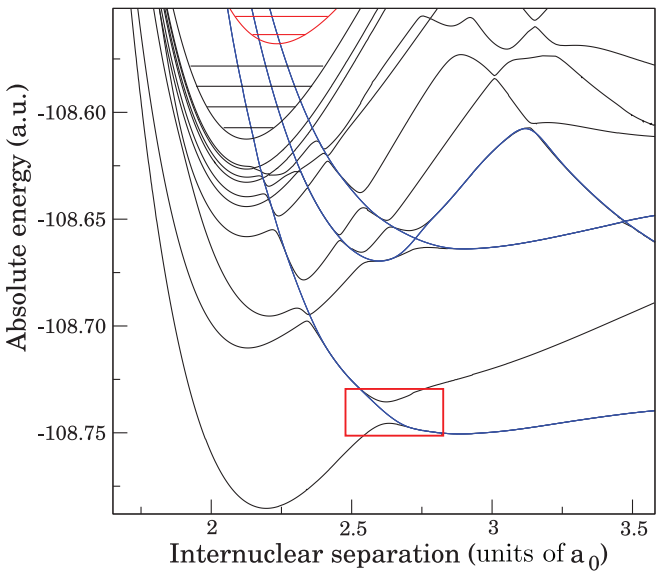

FIG. 1. (Color online) Example of spline fitting to the data given in I, in this case for the symmetry $^3\Pi_u$. The avoiding crossings are interpolated across using a smoothing spline, no formal diabatization is performed. The avoided crossing discussed in Sec. V D is highlighted by the red box.

B. Electronic couplings

For a DR calculation including multiple ionic cores it is necessary to use two types of coupling: Rydberg-valence couplings, which describe the coupling of the ionization channels to valence or dissociative states, and Rydberg-Rydberg couplings, which describe the coupling between ionization channels of a given symmetry associated with each ionic state. All couplings used in the present calculation are given in the Supplemental Material [44].

1. Rydberg-valence couplings

Resonances were calculated using the time-delay method of Smith [30] using the module TIMEDEL with an improved fitting method [20,27]. In classical terms the time delay of a scattered electron can be thought of as the difference in time an electron would experience with or without an interaction with the target. Resonances appear as Lorentzians when the eigenvalues of the time-delay matrix are plotted against energy. These Lorentzians are fitted to find the autoionization width, $\Gamma(R)$, of the resonance, where R is internuclear separation. The autoionization width is then transformed into a Rydberg-valence coupling using $V(R) = \sqrt{\Gamma(R)/2\pi}$. The time-delay method also provides the branching ratio of the autoionization to a partial wave through the square of the time-delay matrix eigenvector [31]. This means that the coupling can be resolved by autoionization to a specific electronic state of the ion and then again to a specific partial wave associated with that state. In this study we only resolved the coupling to autoionize into a particular electronic state of the ion; see Fig. 4. Indeed, this was necessary to correctly include the coupling to each ionic core included in the cross-section calculation.

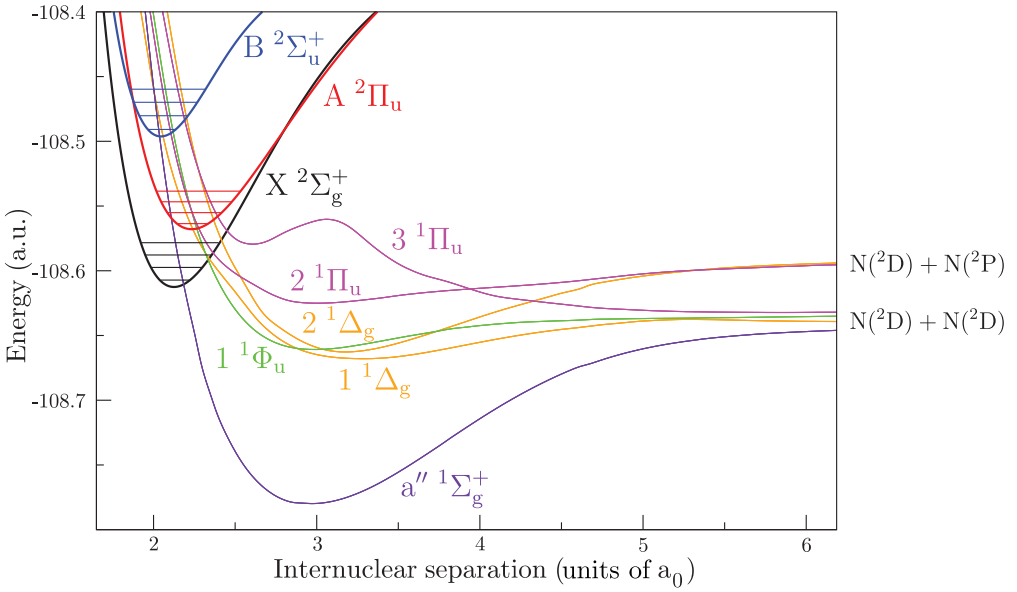

FIG. 2. (Color online) Singlet dissociative states included in the cross-section calculation with their asymptotic limits. The potential-energy curves were taken from the data provided by I and II.

Again, due to the reasons outlined in Sec. II A regarding the avoided crossings and gaps in data, it was necessary to fit the couplings with smoothing splines; an example is given in Fig. 4. There is a significant amount of structure in the couplings due to the adiabatic behavior of the dissociative state interacting with Rydberg states as it passes through them; this structure was ignored, which can be thought of as a "diabatization of the couplings." For more details on the adiabatic structure of the couplings, see Sec. 5.2 of II.

In the *R*-matrix method the electronic width of a resonance goes to zero below the ground state of the ion. Therefore, couplings were forced to zero rapidly after the threshold had been crossed; see Fig. 4. The couplings associated with each dissociative state are displayed in Fig. 5 and Fig. 6 for singlet and triplet states, respectively.

2. *Rydberg-Rydberg couplings*

Rydberg-Rydberg couplings were found for the interaction between the Rydberg series with the lowest value of ℓ converging on the *X* state and the Rydberg state with the lowest value of n and ℓ converging on the *A* state. Rydberg-Rydberg couplings for the *B* state interacting with the *X* state were not included in the calculation as the only interaction was at very

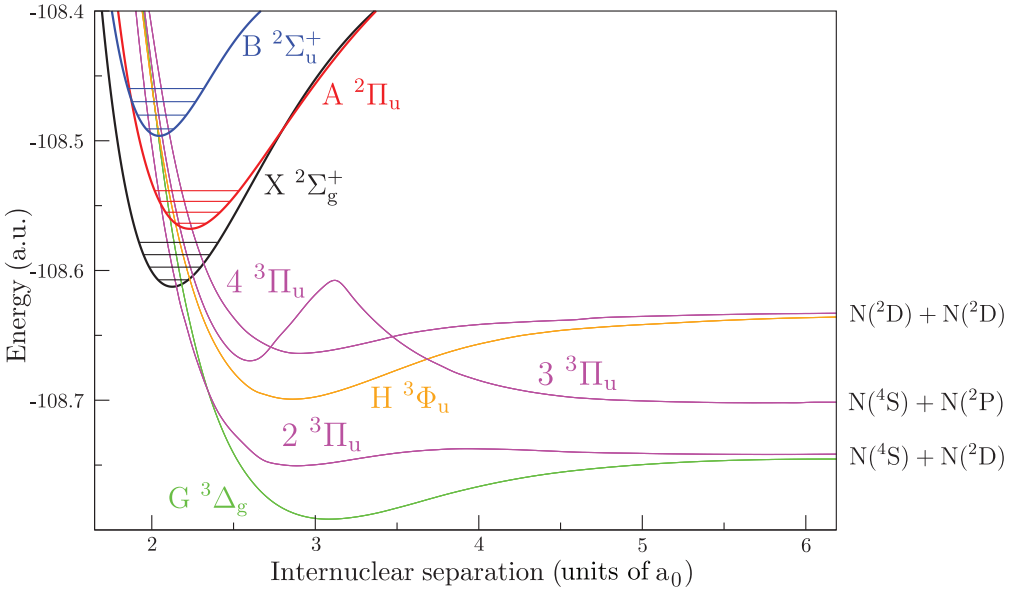

FIG. 3. (Color online) Triplet dissociative states included in the cross-section calculation with their asymptotic limits. The potential-energy curves were taken from the data provided in I and II.

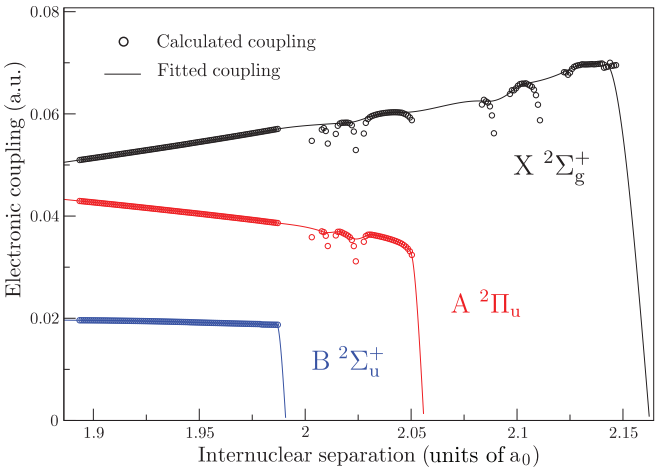

FIG. 4. (Color online) Example of the fitted couplings, in this case of $^3\Pi_u$ symmetry. The total coupling has been resolved by the autoionization branching ratios to the state of the ion to which they are coupled (black, red, blue for X, A, B). The couplings show considerable structure due to the adiabatic nature of the states they are associated with. This structure was ignored and the gaps interpolated across using smoothing splines. The structure of the couplings is discussed in more detail in II.

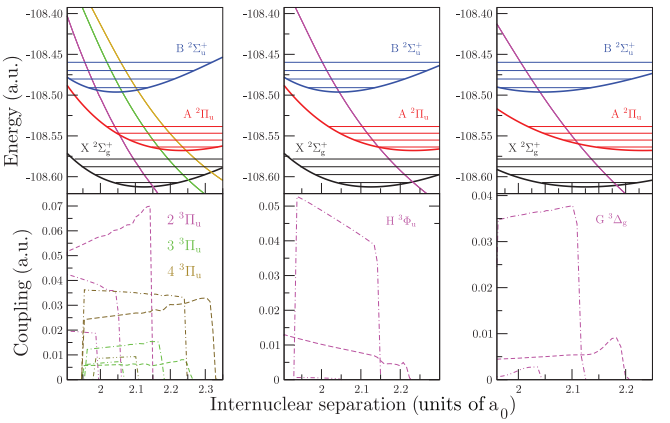

FIG. 6. (Color online) Potential-energy curves of triplet states (top panel) and their respective Rydberg-valence coupling (lower panel). The couplings are resolved by the ionic state to which they are coupled; X state — — —; A state – • – •; B state — •• — ••.

short internuclear separations. The implementation of MQDT used only supports Rydberg-Rydberg couplings between the ground and excited states and hence couplings between the A and B state were not included in the calculation. The couplings were calculated by assuming a two-state interaction with adiabatic potential-energy matrix $\mathbf{V}$ between the two adiabatic Rydberg state potentials with matrix elements $V(R)_{ij} = V_i(R)\delta_{ij}$. This can be transformed to a diabatic potential matrix $\mathbf{U}$ with a 2×2 rotation matrix $\mathbf{R}$ using $\mathbf{U} = \mathbf{R}^{-1}\mathbf{V}\mathbf{R}$. The off-diagonal elements of the diabatic potential matrix $U_{12} = U_{21} = \frac{1}{2}[V(R)_{22} - V(R)_{11}]\sin[2\gamma(R)]$ then gives the

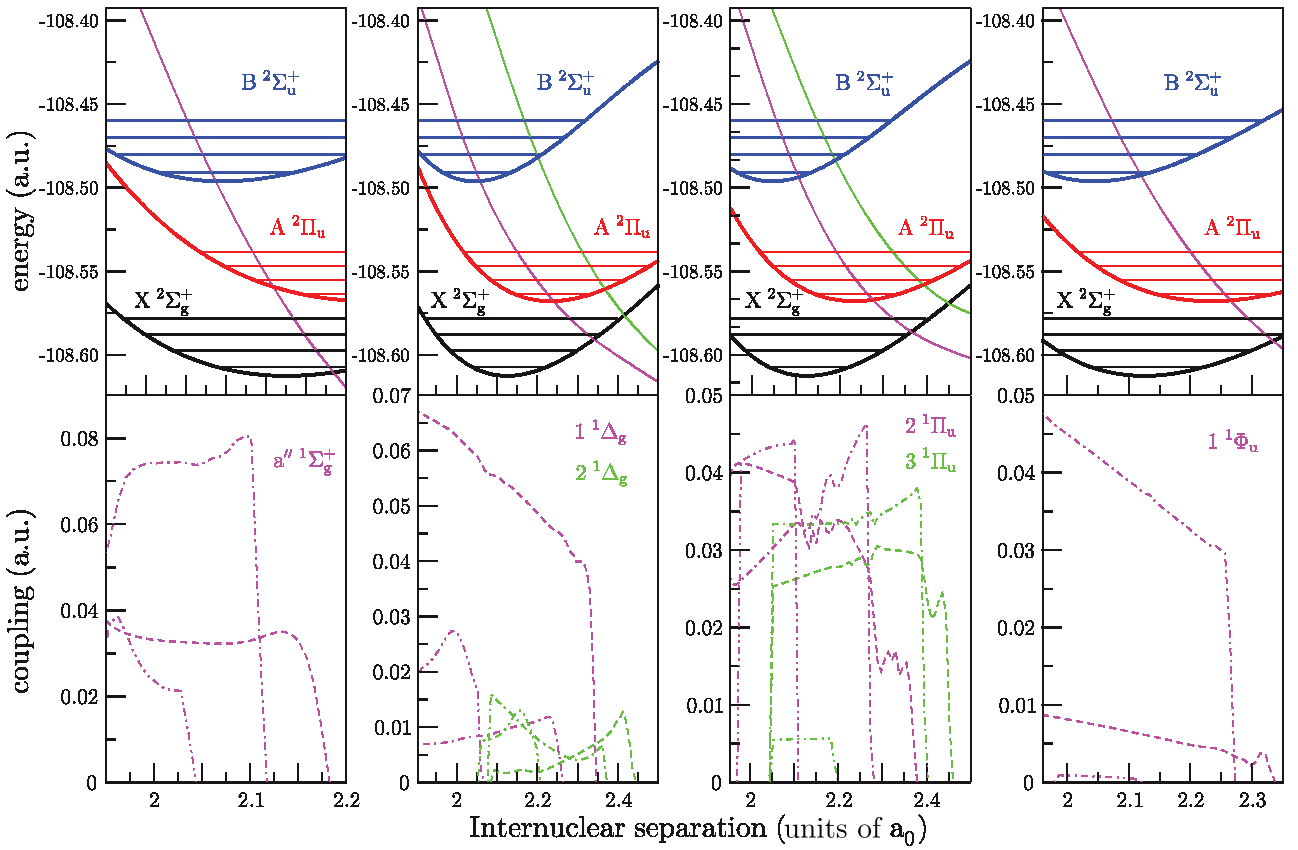

FIG. 5. (Color online) Potential-energy curves of singlet states (top panel) and their respective Rydberg-valence coupling (lower panel). The couplings are resolved by the ionic state to which they are coupled; X state — — —; A state —•—; B state —••—.

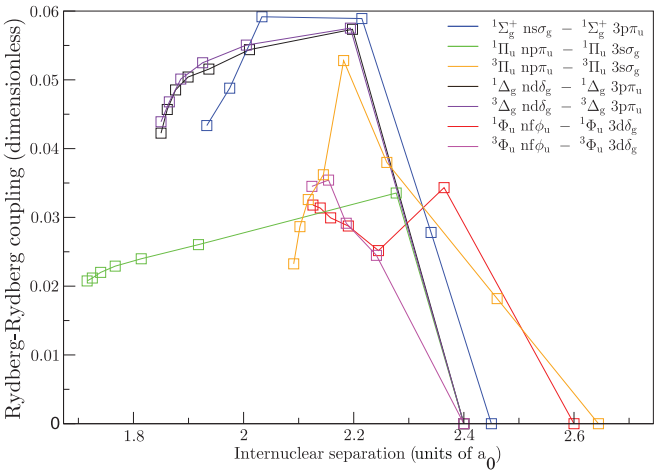

FIG. 7. (Color online) Rydberg-Rydberg couplings for each symmetry included in the cross-section calculation. The couplings associated with Rydberg states with $n \geqslant 5$ are only approximate; see text.

unscaled electronic coupling between the two states where γ is the rotation angle. If the energetic point of closest approach occurs at the same R, then $\gamma = \pi/4$ and the coupling is simply half the difference between the adiabatic states [32]. The coupling is then scaled according to the scaling law

$$\tilde{U}_{n_i n_j} = \sqrt{n_i^{*3} n_j^{*3}}\, U_{n_i n_j} \tag{2}$$

(in atomic units), where i and j correspond to each core state, and n^* is the effective quantum number associated with each Rydberg state [33].

In our data the point of closest approach only occurs at the same value of R for Rydberg states of low n. For interactions between Rydberg states of higher n ($\geqslant$5), the coupling was approximated by taking half the difference between the adiabatic potentials at the value of R halfway between the point of closest approach. The couplings were assumed to go to zero at a point where the X Rydberg series and A Rydberg state were clearly no longer interacting, usually $\sim$0.2 a_0 away from the energetically lowest avoided crossing. The Rydberg-Rydberg couplings used in the calculation are plotted in Fig. 7.

C. Quantum defects

In an MQDT calculation the quantum defect is interpolated to the scattering phase shift and therefore, ideally, quantum defects associated with the highest value of n should be used. Computing quantum defects of high n can be problematic for standard configuration-interaction (CI) techniques as they decrease in accuracy with increasing energy. As a result averages are taken of the quantum defect over the entire series [33].

The R-matrix method has a distinct advantage in that the highest n Rydberg states are the most accurate, as shown in Table 1 of II. Therefore, for this calculation the quantum defect for the highest value of n was used. Limitations were placed on this value by the energetic proximity of the A state to the X state which results in Rydberg states interacting close to the threshold. This, coupled with the energy difference between states scaling with $1/n^2$, makes it difficult to confidently identify high n Rydberg states over a large enough range of internuclear separations, $\sim$1.5–3.5 a.u. Nevertheless, for all symmetries, quantum defects with $n \geqslant 7$ state were successfully used.

III. MQDT-TYPE APPROACH TO LOW-ENERGY DISSOCIATIVE RECOMBINATION WITH CORE EXCITED STATES

A. MQDT formalism for a single-ion core

We restrict ourselves to the case where the energy of the incident electron is lower than the dissociation energy of the target ion, considered to be in its ground electronic state. The collision process involves two mechanisms: (a) the direct process, where the incoming electron is captured in a doubly excited neutral dissociative state N_2^{**}, which either autoionizes or leads to two N neutral fragments

$$N_2^+(v_i^+) + e^- \rightarrow N_2^{**} \rightarrow \begin{cases} N + N^*, \\ N_2^+(v_f^+) + e^-, \end{cases} \tag{3}$$

and (b) the indirect process, where the incident electron is temporarily captured into a singly excited bound Rydberg state N_2^*, predissociated by N_2^{**}:

$$\begin{aligned} N_2^+(v_i^+) + e^- &\rightarrow N_2^* \rightarrow N_2^{**}, \\ N_2^{**} &\rightarrow \begin{cases} N + N^*, \\ N_2^+(v_f^+) + e^-. \end{cases} \end{aligned} \tag{4}$$

Both direct and indirect processes involve two different types of channels, namely dissociation and ionization channels. A channel is open if the total energy of the molecular system is higher than the energy of its fragmentation threshold, and closed in the opposite case. A closed ionization channel introduces in the calculation a series of Rydberg states differing only by the principal quantum number of the external electron [34]. Hence the inclusion of the closed channels allows for the indirect mechanism, which interferes with the direct mechanism resulting in the total process.

The short-range Rydberg-valence interaction couples the dissociation and ionization channels. For a given symmetry Λ of the neutral system, assuming that one single partial wave of the incident electron contributes to this interaction, the R-dependent electronic coupling of an ionization channel relying on the ground-state electronic core c_1 with the dissociation channel d_j is written [35]:

$$\mathcal{V}_{d_j,c_1}^{(e)\Lambda}(R) = \left\langle \Phi_{d_j} \middle| H_{\rm el} \middle| \Phi_{c_1}^{\rm el/ion} \right\rangle, \tag{5}$$

is assumed to be independent of the energy of the external electron, and the integration is performed over the electronic coordinates of the neutral (electron + ion) system. Here $H_{\rm el}$ denotes the electronic Hamiltonian, Φ_{d_j} is the electronic wave function of the dissociative state, and $\Phi_{c_1}^{\rm el/ion}$ the wave function describing the electron-ion system, the ion being in its electronic ground state, c_1. Integrating these couplings over the internuclear distance, the nonvanishing elements of the interaction matrix $\boldsymbol{V}(E)$ are

$$V_{d_j,v}^{\Lambda}(E) = \left\langle F_{d_j}(E) \middle| \mathcal{V}_{d_j,c_1}^{(e)\Lambda}(R) \middle| \chi_v \right\rangle. \tag{6}$$

Here χ_v is the vibrational wave function associated with an ionization channel in the reaction zone, F_{d_j} is the radial wave function of the dissociative state d_j, and E is the total energy of the molecular system. This interaction is effective at short electron-ion and internuclear distances typical in the reaction zone.

Starting with the interaction matrix $\boldsymbol{V}$, a short-range reaction matrix, $\mathcal{K}$, is then built as a solution of the Lippmann-Schwinger equation

$$\mathcal{K} = \boldsymbol{V} + \boldsymbol{V}\frac{\mathbf{1}}{\boldsymbol{E} - \boldsymbol{H_0}}\mathcal{K}, \tag{7}$$

where H_0 is the zero-order Hamiltonian of the molecular system.

The structure of the reaction matrix $\mathcal{K}$ in block form is

$$\mathcal{K} = \begin{pmatrix} \mathcal{K}_{\bar{d}\bar{d}} & \mathcal{K}_{\bar{d}\bar{v}} \\ \mathcal{K}_{\bar{v}\bar{d}} & \mathcal{K}_{\bar{v}\bar{v}} \end{pmatrix}, \tag{8}$$

where the collective indices $\bar{d}$ and $\bar{v}$ span the ensembles of all individual indices d_j and v which respectively label dissociation channels and ionization channels built on core c_1.

For an energy-independent coupling $V(R)$, Eq. (7) has a perturbative solution which is exact to second order [36]:

$$\mathcal{K} = \begin{pmatrix} \mathbf{O} & \boldsymbol{V}_{\bar{d}\bar{v}} \\ \boldsymbol{V}_{\bar{v}\bar{d}} & \mathcal{K}^{(2)}_{\bar{v}\bar{v}} \end{pmatrix}. \tag{9}$$

Here $\mathbf{O}$ is the null matrix and the elements of the diagonal block $\mathcal{K}^{(2)}_{\bar{v}\bar{v}}$ of $\mathcal{K}$ are given by

$$K^{(2)}_{vv'} = \sum_{d_j}\frac{1}{W_{d_j}}\iint\left[\chi^{\Lambda}_{v}(R)\mathcal{V}_{d_j}(R)F_{d_j}(R_<)\right. \\ \left.\times G_{d_j}(R_>)\mathcal{V}_{d_j}(R')\chi^{\Lambda}_{v'}(R')\right]dR\,dR'. \tag{10}$$

where W_{d_j} is the Wronskian of the function pair (F_{d_j}, G_{d_j}), and $\mathcal{V}_{d_j}(R)$ is a simplified notation for the coupling defined in Eq. (5).

To express the effects of short-range interactions in terms of phase shifts we diagonalize the $\mathcal{K}$ matrix

$$\mathcal{K}\mathcal{U} = -\frac{1}{\pi}\tan(\boldsymbol{\eta})\mathcal{U}, \tag{11}$$

where $\boldsymbol{\mathcal{U}}$ is a matrix whose columns are eigenvectors of matrix $\mathcal{K}$ and the diagonal matrix $\tan(\boldsymbol{\eta})$ contains its eigenvalues.

In the external region, where the Born-Oppenheimer representation is no longer valid for the neutral molecule, a frame transformation [35] is performed via the projection coefficients

$$\mathcal{C}_{v^+,\Lambda\alpha} = \sum_{v} U^{\Lambda}_{v,\alpha}\langle\chi_{v^+}(R)|\cos\left[\pi\mu^{\Lambda}_{c_1}(R) + \eta^{\Lambda}_{\alpha}\right]|\chi_v(R)\rangle, \tag{12}$$

$$\mathcal{C}_{d_j,\Lambda\alpha} = U^{\Lambda}_{d_j,\alpha}\cos\eta^{\Lambda}_{\alpha}, \tag{13}$$

$$\mathcal{S}_{v^+,\Lambda\alpha} = \sum_{v} U^{\Lambda}_{v,\alpha}\langle\chi_{v^+}(R)|\sin\left[\pi\mu^{\Lambda}_{c_1}(R) + \eta^{\Lambda}_{\alpha}\right]|\chi_v(R)\rangle, \tag{14}$$

$$\mathcal{S}_{d_j,\Lambda\alpha} = U^{\Lambda}_{d_j,\alpha}\sin\eta^{\Lambda}_{\alpha}, \tag{15}$$

where α denotes the eigenchannels built through diagonalization of the reaction matrix $\mathcal{K}$. These can be grouped into matrices $\boldsymbol{\mathcal{C}}$ and $\boldsymbol{\mathcal{S}}$ which are the building blocks of the generalized scattering matrix $\boldsymbol{X}$ that involves all open ("o") and closed ("c") channels. The $\boldsymbol{X}$ matrix in turn can be arranged into four submatrices

$$\boldsymbol{X} = \frac{\boldsymbol{\mathcal{C}} + i\boldsymbol{\mathcal{S}}}{\boldsymbol{\mathcal{C}} - i\boldsymbol{\mathcal{S}}} = \begin{pmatrix} \boldsymbol{X_{oo}} & \boldsymbol{X_{oc}} \\ \boldsymbol{X_{co}} & \boldsymbol{X_{cc}} \end{pmatrix}. \tag{16}$$

Imposing boundary conditions leads to the physical scattering matrix [37]:

$$\boldsymbol{S} = \boldsymbol{X_{oo}} - \boldsymbol{X_{oc}}\frac{\mathbf{1}}{\boldsymbol{X_{cc}} - \exp(-i2\pi\boldsymbol{\nu})}\boldsymbol{X_{co}}, \tag{17}$$

where the diagonal matrix $\boldsymbol{\nu}$ is constructed with the effective quantum numbers $\nu_{v^+} = [2(E_{v^+} - E)]^{-1/2}$ (in atomic units) associated with each vibrational threshold E_{v^+} of the ion, situated above the current total energy E, labeling a closed channel.

For a molecular ion, initially in the vibrational state v_i^+, recombining with an electron of energy ε, the cross section of capture into all the dissociative states d_j of the same symmetry Γ (gerade or ungerade, singlet or triplet) and electronic angular momentum projection Λ can be written as

$$\sigma^{\Gamma,\Lambda}_{\mathrm{diss}\leftarrow v_i^+} = \frac{\pi}{4\varepsilon}\rho^{\Gamma,\Lambda}\sum_{j}\left|S_{d_j,v_i^+}\right|^2, \tag{18}$$

where $\rho^{\Gamma,\Lambda}$ is the ratio between the spin multiplicities of the neutral and the target ion. The total cross section for DR is obtained by summing over all available Γ,Λ:

$$\sigma^{\mathrm{sym}}_{\mathrm{diss}\leftarrow v_i^+} = \sum_{\Gamma,\Lambda}\sigma^{\Gamma,\Lambda}_{\mathrm{diss}\leftarrow v_i^+}. \tag{19}$$

B. Inclusion of core excited states

The MQDT formalism in the previous section is valid for a system where one or more dissociative states are coupled to the ionization channels of the ground ion core. However, N_2^+ has several bound excited states whose ionization continua are coupled to the ionization continuum of the ground core and to neutral dissociative states.

For the energy range characterizing the incident electron in the present work, two such excited states, $A\ ^2\Pi_u$ and $B\ ^2\Sigma_u^+$, are relevant, which we call core 2 and core 3, respectively. The neutral dissociative states $2\ ^3\Pi_u$, $3\ ^3\Pi_u$, and $4\ ^3\Pi_u$ are coupled to the ionization channels of the three ion cores and are responsible for driving the low-energy DR mechanism. Figure 8 shows the curves used in the present calculation that were taken from I and II and discussed in the previous section.

The interaction between the ionization and dissociation channels results in two types of couplings, namely the Rydberg-valence couplings defined in Eqs. (5) and (6) and those built in a similar way for the excited cores c_2 and c_3:

$$V^{\Lambda}_{d_j,w}(E) = \left\langle F_{d_j}(E)\middle|\mathcal{V}^{(e)\Lambda}_{d_j,c_2}(R)\middle|\chi_w\right\rangle, \tag{20}$$

$$V^{\Lambda}_{d_j,u}(E) = \left\langle F_{d_j}(E)\middle|\mathcal{V}^{(e)\Lambda}_{d_j,c_3}(R)\middle|\chi_u\right\rangle, \tag{21}$$

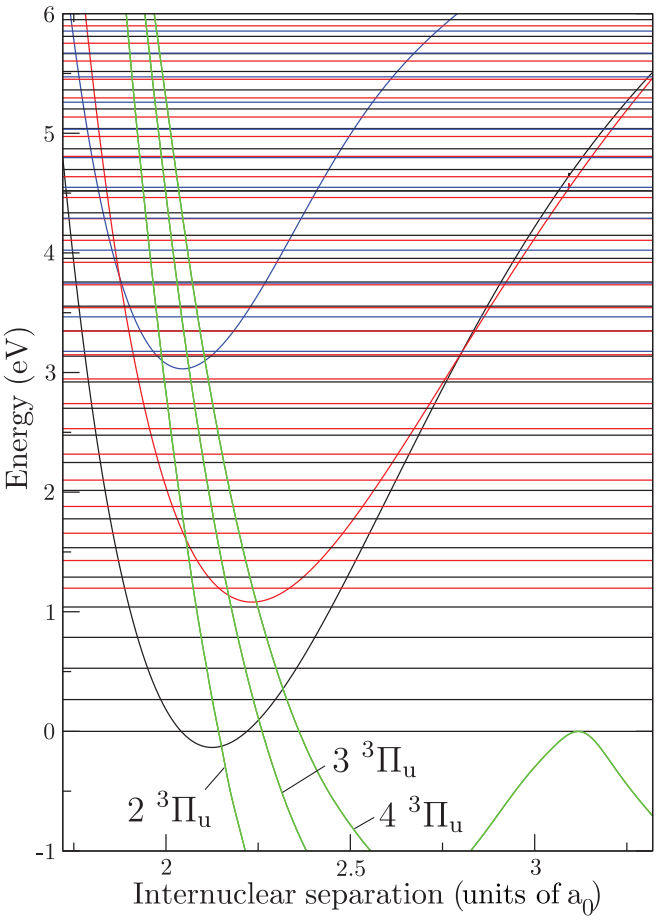

FIG. 8. (Color online) N_2^+/N_2 states relevant for the electron-N_2^+ dissociative recombination and vibrational excitation. Potential-energy curves for N_2^+ $X\ ^2\Sigma_g^+$ (lowest curve, black), N_2^+ $A\ ^2\Pi_u$ (middle curve, red), N_2^+ $B\ ^2\Sigma_u^+$ (topmost curve, blue), and N_2 $2\ ^3\Pi_u$, $3\ ^3\Pi_u$, $4\ ^3\Pi_u$ dissociative states (green, labeled). The vibrational levels of the ground and excited cores are represented by horizontal thin lines, of the same color as that of the respective ion cores. Zero energy is defined as the ground-state vibrational level of $X\ ^2\Sigma_g^+$.

and the Rydberg-Rydberg couplings given by [33]

$$V^{\Lambda}_{vw} = \langle\chi_v|\widetilde{\mathcal{V}}^{(e)\Lambda}_{c_1,c_2}(R)|\chi_w\rangle, \tag{22}$$

$$V^{\Lambda}_{vu} = \langle\chi_v|\widetilde{\mathcal{V}}^{(e)\Lambda}_{c_1,c_3}(R)|\chi_u\rangle, \tag{23}$$

$$V^{\Lambda}_{wu} = \langle\chi_w|\widetilde{\mathcal{V}}^{(e)\Lambda}_{c_2,c_3}(R)|\chi_u\rangle, \tag{24}$$

where the vibrational quantum numbers v, w, and u label the ionization channels of core 1, 2, and 3, respectively.

The structure of the reaction matrix $\mathcal{K}$ in block form is the following:

$$\mathcal{K} = \begin{pmatrix} \mathcal{K}_{\bar{d}\bar{d}} & \mathcal{K}_{\bar{d}\bar{v}} & \mathcal{K}_{\bar{d}\bar{w}} & \mathcal{K}_{\bar{d}\bar{u}} \\ \mathcal{K}_{\bar{v}\bar{d}} & \mathcal{K}_{\bar{v}\bar{v}} & \mathcal{K}_{\bar{v}\bar{w}} & \mathcal{K}_{\bar{v}\bar{u}} \\ \mathcal{K}_{\bar{w}\bar{d}} & \mathcal{K}_{\bar{w}\bar{v}} & \mathcal{K}_{\bar{w}\bar{w}} & \mathcal{K}_{\bar{w}\bar{u}} \\ \mathcal{K}_{\bar{u}\bar{d}} & \mathcal{K}_{\bar{u}\bar{v}} & \mathcal{K}_{\bar{u}\bar{w}} & \mathcal{K}_{\bar{u}\bar{u}} \end{pmatrix}, \tag{25}$$

where the collective indices $\bar{d}$, $\bar{v}$, $\bar{w}$, $\bar{u}$ span the ensembles of all individual indices d_j, v, w, and u which respectively label dissociation channels and ionization channels built on core 1, core 2, and core 3.

An extensive and rigorous derivation of the structure of each block of the $\mathcal{K}$ matrix in second order was provided in our earlier work [38] on H_2^+/HD^+ with two cores, where in addition to the H_2^+/HD^+ ground core there was a repulsive ion core. For N_2^+, with three attractive ion cores, natural extensions of our earlier work lead to the following form of the $\mathcal{K}$ matrix to second order,

$$\mathcal{K} = \begin{pmatrix} \mathbf{O} & \boldsymbol{V}_{\bar{d}\bar{v}} & \boldsymbol{V}_{\bar{d}\bar{w}} & \boldsymbol{V}_{\bar{d}\bar{u}} \\ \boldsymbol{V}_{\bar{v}\bar{d}} & \boldsymbol{\mathcal{K}}^{(2)}_{\bar{v}\bar{v}} & \boldsymbol{V}_{\bar{v}\bar{w}} & \boldsymbol{V}_{\bar{v}\bar{u}} \\ \boldsymbol{V}_{\bar{w}\bar{d}} & \boldsymbol{V}_{\bar{w}\bar{v}} & \boldsymbol{\mathcal{K}}^{(2)}_{\bar{w}\bar{w}} & \boldsymbol{V}_{\bar{w}\bar{u}} \\ \boldsymbol{V}_{\bar{u}\bar{d}} & \boldsymbol{V}_{\bar{u}\bar{v}} & \boldsymbol{V}_{\bar{u}\bar{w}} & \boldsymbol{\mathcal{K}}^{(2)}_{\bar{u}\bar{u}} \end{pmatrix}, \tag{26}$$

where the elements of the diagonal blocks of $\mathcal{K}$ are written

$$K^{(2)}_{aa'} = \sum_{d_j} \frac{1}{W_{d_j}} \iint \left[\chi^{\Lambda}_a(R)\mathcal{V}_{d_j}(R)F_{d_j}(R_<) \times G_{d_j}(R_>)\mathcal{V}_{d_j}(R')\chi^{\Lambda}_{a'}(R')\right] dR\, dR', \tag{27}$$

where, as before, a stands for either v, w, or u and a' denotes the corresponding primed quantities, and $\mathcal{V}_{d_j}(R)$ is a simplified notation for the couplings appearing in Eqs. (6), (20), and (21).

C. Calculation of cross sections

The inclusion of the additional excited ion cores increases not only the dimension of the $\mathcal{K}$ matrix, Eq. (9), but also that of the $\mathcal{C}$ and $\mathcal{S}$ matrices. More specifically, besides the matrix elements given by Eqs. (12) and (14), further matrix elements related to cores 2 and 3 contribute to the building of these matrices:

$$\mathcal{C}_{w^+,\Lambda\alpha} = \sum_w U^{\Lambda}_{w,\alpha}\langle\chi_{w^+}(R)|\cos\left[\pi\mu^{\Lambda}_{c_2}(R) + \eta^{\Lambda}_{\alpha}\right]|\chi_w(R)\rangle, \tag{28}$$

$$\mathcal{S}_{w^+,\Lambda\alpha} = \sum_w U^{\Lambda}_{w,\alpha}\langle\chi_{w^+}(R)|\sin\left[\pi\mu^{\Lambda}_{c_2}(R) + \eta^{\Lambda}_{\alpha}\right]|\chi_w(R)\rangle, \tag{29}$$

$$\mathcal{C}_{u^+,\Lambda\alpha} = \sum_u U^{\Lambda}_{u,\alpha}\langle\chi_{u^+}(R)|\cos\left[\pi\mu^{\Lambda}_{c_3}(R) + \eta^{\Lambda}_{\alpha}\right]|\chi_u(R)\rangle, \tag{30}$$

$$\mathcal{S}_{u^+,\Lambda\alpha} = \sum_u U^{\Lambda}_{u,\alpha}\langle\chi_{u^+}(R)|\sin\left[\pi\mu^{\Lambda}_{c_3}(R) + \eta^{\Lambda}_{\alpha}\right]|\chi_u(R)\rangle, \tag{31}$$

and, consequently, via Eqs. (16) and (17), to the building of the matrices $\mathcal{C}$ and $\mathcal{S}$. The DR cross sections are then obtained from Eq. (19).

IV. COMPUTATIONAL DETAILS

The potential-energy curves included in the calculation were selected based on their crossing point with the ground-state PEC of the ion and the size of their Rydberg-valence

coupling. The R-matrix calculation yielded many more states than those that are included in the calculation; however, most were deemed to make insignificant contributions to the total cross section for the energy range studied. There is also some ambiguity as to whether previously unidentified states are valence states or Rydberg states converging to the $a\ ^4\Sigma_u^+$ state of the ion.

Eleven dissociative states of singlet and triplet symmetry were included in the calculation, see Figs. 2 and 3, with couplings resolved to each state of the ion; see Figs. 5 and 6. Cross sections were calculated for $v_i^+ = 0$–3 with an energy range 10^{-5}–1 eV. Ionization channels associated with the X, A and B states were included in the calculation. Only the X and A ionization channels were coupled as the X-B Rydberg-Rydberg coupling is only important at very short bond lengths and was deemed negligible. The cross-section calculation was performed for each symmetry of the neutral individually and then summed to find the total cross section. The integration of Eq. (6) was performed from 0.5 to 25.0 a_0.

V. RESULTS AND DISCUSSION

A. Cross sections

The DR cross section of N_2^+ in its electronic ground state, X, in initial vibrational levels $v_i^+ = 0$–3 can be seen in Fig. 9 and at a larger scale for $v_i^+ = 0$ in Fig. 10. What is immediately obvious from Fig. 10 is that the cross section is dominated by the $^3\Pi_u$ symmetry, in particular the 2 $^3\Pi_u$ state. This is unsurprising considering the state's position close to the turning point of the ion ground state, its large coupling, see Fig. 11, and previous theoretical results by Guberman [15–18] and the experimental results of Kella *et al.* [39].

Secondly, the $N_2^+(v_i^+ = 1)$ DR rate is significantly lower than that for $v_i^+ = 0,2,3$. If one considers that the dominant state in the cross section is the 2 $^3\Pi_u$ state, then this is also to be expected. The crossing point of this state with the ion ground state is very close to the minimum in the ion curve; therefore, for $v_i^+ = 1$, the overlap of the wave function of this state and the vibrational wave function will be significantly reduced due to the node in the vibrational wave function. This effect is

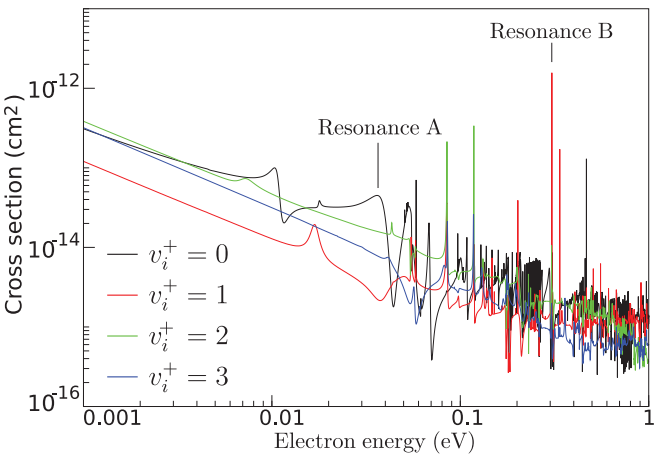

FIG. 9. (Color online) Computed N_2^+ dissociative recombination cross section as a function of cation vibrational state, v_i^+.

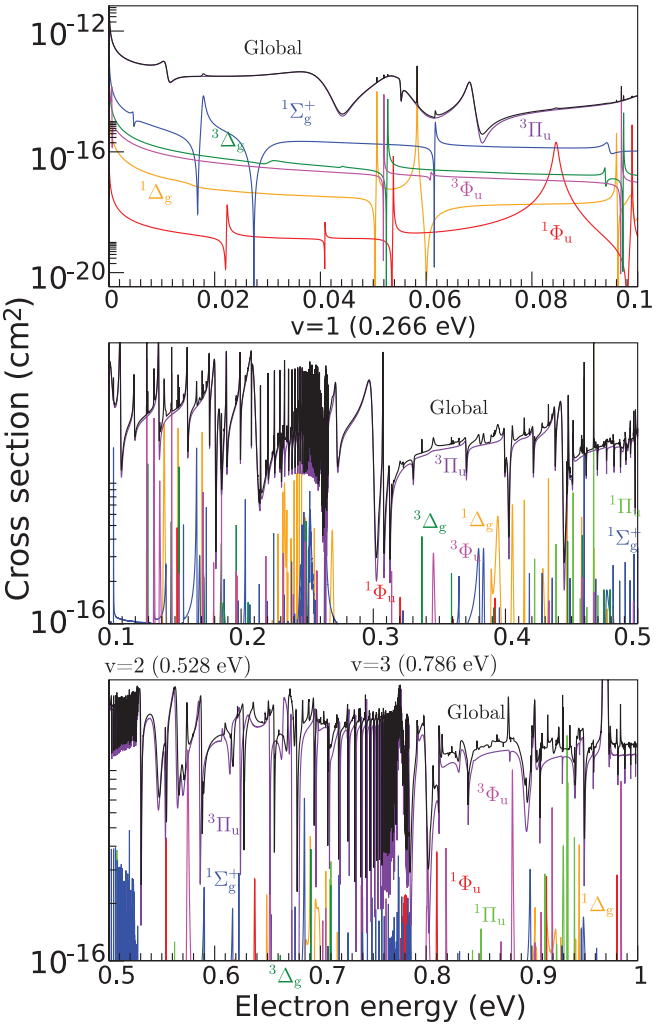

FIG. 10. (Color online) Contribution of different dissociative curves of N_2^{**} to the $N_2^+(v_i^+ = 0)$ DR cross section as a function of energy.

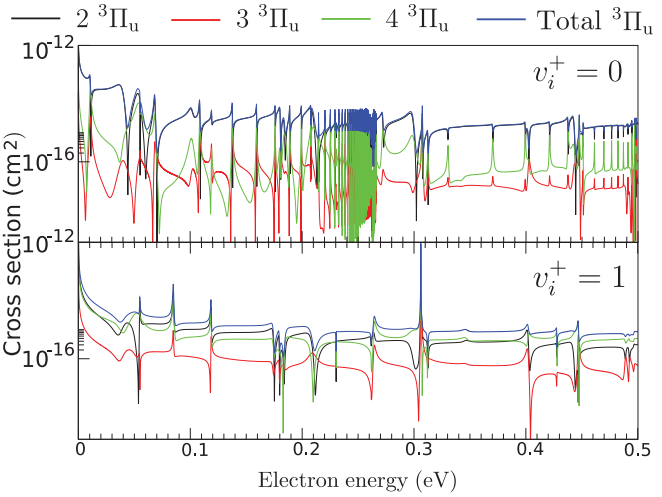

FIG. 11. (Color online) Contribution to the DR cross section of N_2^+ for $v_i^+ = 0$ (top) and $v_i^+ = 1$ (bottom) from N_2^{**} states of $^3\Pi_u$ symmetry.

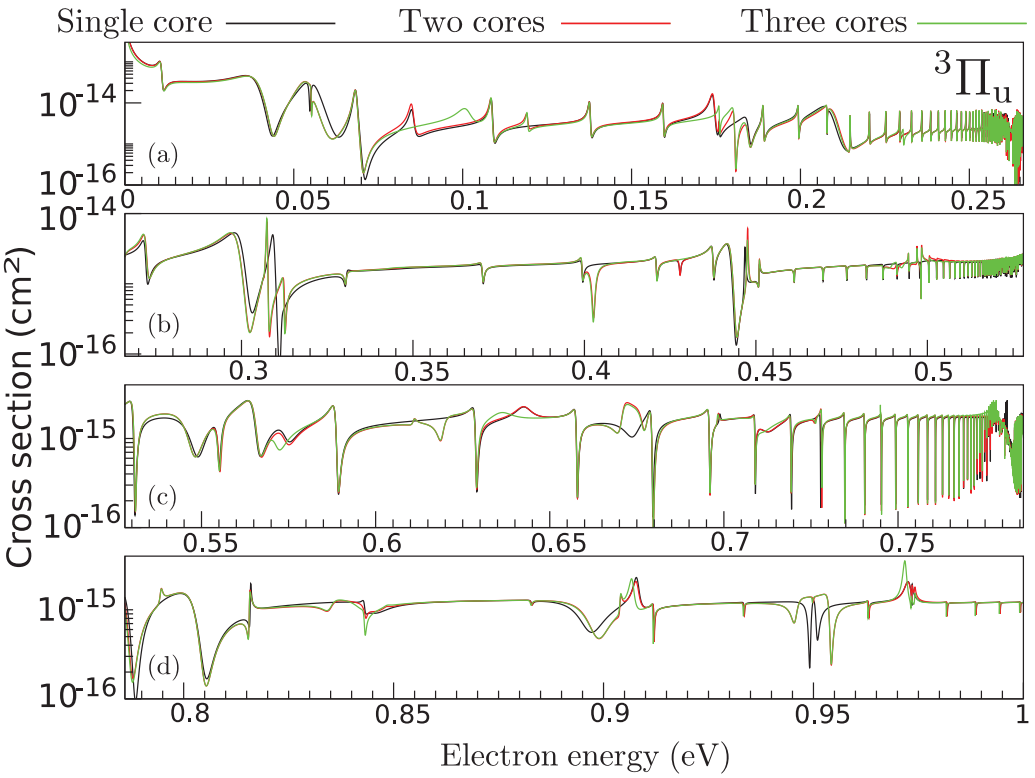

FIG. 12. (Color online) Effect of including multiple cores on the cross-section calculation for $^3\Pi_u$ symmetry. Each panel, with exception of the final, ends at a vibrational threshold. That is, (a) 10^{-5} eV, $v_i^+ = 1$ (0.266 eV), (b) $v_i^+ = 1$ (0.266 eV), $v_i^+ = 2$ (0.528 eV), (c) $v_i^+ = 3$ (0.528 eV), $v_i^+ = 4$ (0.786 eV), and (d) $v_i^+ = 4$ (0.786 eV), 1 eV. Including the second and third core only has a minor effect on the cross section as, for the dominant dissociative state 2 $^3\Pi_u$, the majority of the Rydberg-valence coupling is to the ground state; see the leftmost panel of Fig. 6.

illustrated in Fig. 11. For $v_i^+ = 0$, the contribution to the total cross section from the 3 and 4 $^3\Pi_u$ states is almost negligible in comparison to 2 $^3\Pi_u$. For $v_i^+ = 1$, the 2 and 4 $^3\Pi_u$ states have a similar level of contribution to the overall cross section. This is in agreement with previous studies by Guberman that the most important dissociative states for DR are the 2 and 4 $^3\Pi_u$. For $v_i^+ = 2,3$ the overlap with the dissociative state wave function increases and the magnitude of the cross section is similar to that of $v_i^+ = 0$.

States of other symmetry which cross within $v_i^+ = 0$ are $a''\,^1\Sigma_g^+$ and $G^3\Delta_g$; Figs. 5 and 6 show that although the total width of these states is large, consideration of the autoionization branching ratios shows that the majority of the coupling is to the A state rather than the X state, resulting in a reduced DR cross section.

All other states included in the calculation either have a small coupling to the X state, or cross the ground state far from the turning point, or both and as a result make only minor relative contributions to the cross section. The $^1\Pi_u$ channel does not open until 0.397 eV. Therefore, in a high-resolution measurement of the DR cross section we expect that the majority of the structure will be due to the 2 $^3\Pi_u$ with only narrow resonance peaks due to states of other symmetry.

The effect of including additional cores on the cross section can be seen in Figs. 12 and 13 for $v_i^+ = 0$ for $^3\Pi_u$ and $^3\Delta_g$, respectively. For $^3\Pi_u$ the cross section does not change significantly with the addition of each core to the calculation; there are only slight shifts in the resonance structure, with the most significant change occurring with the inclusion of the third core. This is to be expected as the majority of the coupling for the dominant dissociative state 2 $^3\Pi_u$ is to the

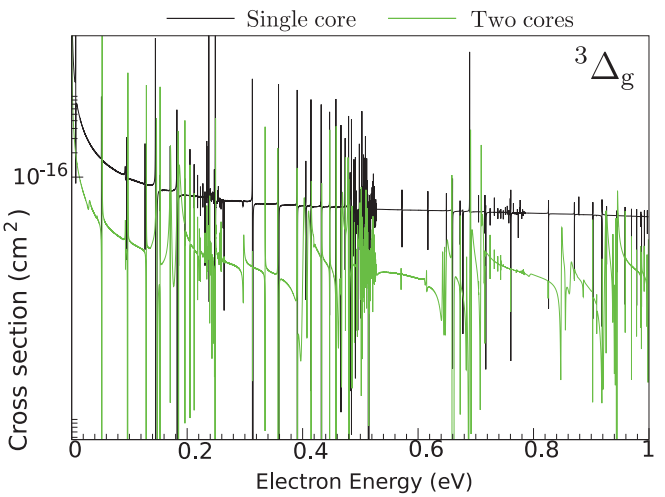

FIG. 13. (Color online) Effect of including multiple cores in the cross-section calculation for $^3\Delta_g$ symmetry. It can be seen in the rightmost panel of Fig. 6 that for this symmetry the majority of Rydberg-valence coupling is to the A state. As a result, the inclusion of the second core has a significant impact on the cross section. The inclusion of the third core makes very little difference to the cross section and resultantly is not shown.

TABLE I. Fitted DR rate coefficients for N_2^+ as function of vibrational state, v_i^+.

v_i^+	Rate coefficient (cm^3s^{-1})	Temperature range (K)
0	$2.568 \times 10^{-7}(T_e/300)^{-0.5166}$	$300 \leqslant T_e \leqslant 800$
	$1.492 \times 10^{-7}(T_e/800)^{-0.47}$	$800 \leqslant T_e \leqslant 1500$
1	$6.378 \times 10^{-8}(T_e/300)^{-0.239}$	$300 \leqslant T_e \leqslant 500$
	$5.652 \times 10^{-8}(T_e/500)^{-0.17}$	$500 \leqslant T_e \leqslant 800$
	$5.225 \times 10^{-8}(T_e/800)^{-0.075}$	$800 \leqslant T_e \leqslant 1025$
	$5.117 \times 10^{-8}(T_e/1100)^{-0.023}$	$1025 \leqslant T_e \leqslant 1250$
	$5.104 \times 10^{-8}(T_e/1300)^{0.008}$	$1250 \leqslant T_e \leqslant 1500$
2	$2.145 \times 10^{-7}(T_e/300)^{-0.36}$	$300 \leqslant T_e \leqslant 800$
	$1.499 \times 10^{-7}(T_e/800)^{-0.42}$	$800 \leqslant T_e \leqslant 1500$
3	$1.228 \times 10^{-7}(T_e/300)^{-0.50}$	$300 \leqslant T_e \leqslant 600$
	$8.711 \times 10^{-7}(T_e/600)^{-0.4352}$	$600 \leqslant T_e \leqslant 1500$

X state; see the leftmost panel of Fig. 6. The addition of the second core has a much larger impact on the $^3\Delta_g$ cross section; this is because the $G\ ^3\Delta_g$ state is most strongly coupled to the A state; see the rightmost panel of Fig. 6. As $^3\Pi_u$ is the dominant symmetry, the core-excited effects are only present in the minor dissociative channels, such as $G\ ^3\Delta_g$, and are therefore not prevalent in the global cross section.

B. Rate coefficients

Isotropic rate coefficients fitted with the form $A(T_e/T)^{-a}$ are given in Table I; the fits give a good reflection of the temperature dependence within their respective ranges. This fitting form is not particularly suitable for the $v_i^+ = 1$ DR rate as its temperature dependence changes frequently; however, fits were made over shorter energy ranges to compensate. The unfitted rate coefficients are available in the Supplemental Material [44] and can be refitted as desired.

C. Comparison with other work and discussion of vibrational dependence

1. Cross sections

As mentioned in the Introduction, there are a number of difficulties cooling N_2^+ sufficiently so that a measurement can be made of its vibrational ground state. Therefore, to make a correct comparison with experiment, we must first sum the relative proportions of the cross section according to the vibrational distribution of the ions with energy. Only two experimental studies provide vibrational distributions of the ion beam and cross sections, Peterson *et al.* [7] and Sheehan and St. Maurice [8].

The vibrational distribution provided by Sheehan and St. Maurice was not directly measured in their merged beam experiment; instead it was taken from Noren *et al.* [40] but deemed that it should give a "reasonable reflection" of the vibrational population of their ion beam. Peterson *et al.* also did not perform a direct measurement of their vibrational populations either; instead they measured the DR rate times population at zero relative energy of the electron and ion beam. By convoluting the calculated cross section according to the temperature distribution of the ion beam (transversal 0.01 eV and longitudinal 0.0001 eV) using an anisotropic Maxwell electron velocity distribution we can calculate vibrationally resolved rates to find a derived population. The derived population using the rates at 10^{-5} eV is 0.274:0.533:0.066:0.127 $v_i^+ = 0$–3, respectively, for the JIMIS ion source [7]. The vibrational distribution provided by Sheehan and St. Maurice is 0.651:0.211:0.084:0.035:0.013:0.005:0.001 $v_i^+ = 0$–6, respectively.

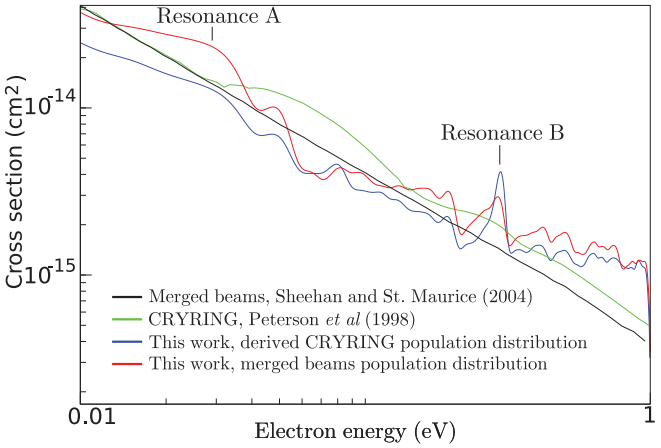

FIG. 14. (Color online) Comparison of our computed N_2^+ DR effective cross sections with those measured using CRYRING [7] and by Sheehan and St. Maurice [8].

Figure 14 gives a comparison of the effective cross sections measured in both experiments with our convoluted calculated cross sections scaled with their respective vibrational populations. The general agreement with experiment is good; in practice, use of the vibrational distribution given by Sheehan and St. Maurice gives better agreement with both measurements than the derived population distribution from Peterson *et al.*

Our calculations show many resonance structures arising from the indirect mechanism. Except where these structures merge together, often in the region of thresholds, these structures are generally averaged by the thermal distribution of the electrons used experimentally. There are two main structures in the CRYRING cross section which are reproduced by our calculation: a broad resonance centered at ~0.07 eV and a smaller resonance structure at ~0.3 eV. These structures are present in the cross section with both population distributions, and are labeled "resonance A" and "resonance B" in Figs. 9 and 14. Our results indicate that each structure comes from a cross section of a different vibrational level: resonance A is from the $v_i^+ = 0$ cross section and resonance B from the $v_i^+ = 1$ cross section; see Fig. 9. This gives a clear theoretical indication that the vibrational distribution is dominated by $v_i^+ = 0$ and $v_i^+ = 1$; our results do not show any large resonance features in $v_i^+ = 2,3$.

Sheehan and St. Maurice make the point that, as their measured cross sections and the CRYRING cross section are similar, the vibrational distribution of the ions may have also been similar in both experiments. This is, of course, only true if the cross section is significantly vibrationally dependent. Our calculation suggests that there is clearly a significant difference between $v_i^+ = 0$ and 1 cross sections, and our cross section

with the Sheehan and St. Maurice population distribution has better agreement with the CRYRING cross section. One, however, must be cautious in making these comparisons as the measurement of the population distribution was not actually carried out on the ion beam of either experiment and population effects are known to have subtle effects on the effective DR cross sections measured, as found, for example, in the DR of H_3^+ [41].

Guberman's most recent study [18] suggests that at very low energies (0.001 eV) the cross sections for each vibrational level are all of a similar magnitude, and in fact that $v_i^+ = 1$ is the largest. Use of these cross sections yields a vibrational distribution of 0.50:0.25:0.10:0.14 for $v_i^+ = 0$–3, respectively, which is similar to that of Sheehan and St. Maurice. From the perspective of our model, the difference between the two studies comes down to the importance of the 4 $^3\Pi_u$ state. In Guberman's model this state is slightly lower in energy and has a Rydberg-valence coupling which is around double the magnitude found by the R-matrix calculations presented in II, dominating the $v_i^+ = 1$ cross section at low energies. In our model the process is driven entirely by the 2 $^3\Pi_u$ which, for reasons described in Sec. V A, leads to a reduced $v_i^+ = 1$ cross section. Unfortunately the data for the cross sections was not available for Guberman's study so we cannot make any direct comparisons of the vibrationally resolved cross sections.

2. *Rate coefficients*

Figure 15 gives a comparison with the flowing afterglow Langmuir probe (FALP) measurements, given as an isotropic rate coefficient, of Mahdavi *et al.* [11], Geoghegan *et al.* [12], and Canosa *et al.* [13], and our $v_i^+ = 0$ isotropic rate coefficient at 300 K [8]. There is very good agreement with our calculated $v_i^+ = 0$ rates and the FALP measurements, the value is within error of the measurement of Canosa *et al.* and Mahdavi, and is just outside the error bars of Geoghegan *et al.*

By comparing the above measurements for $v_i^+ = 0$ and those with a mix of vibrational levels we get another indication that the $v_i^+ = 1$ rate must be lower than $v_i^+ = 0$; the rates where

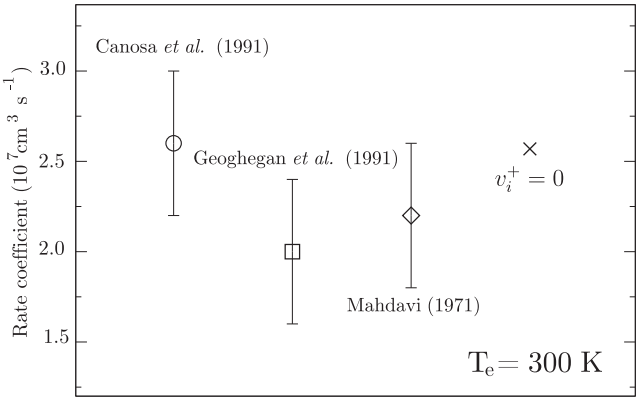

FIG. 15. Comparison of our calculated, isotropic rate coefficient for N_2^+ DR $v_i^+ = 0$ with the FALP measurements of Mahdavi *et al.* [11], Geoghegan *et al.* [12], and Canosa *et al.* [13] at 300 K. Agreement with experiment is excellent.

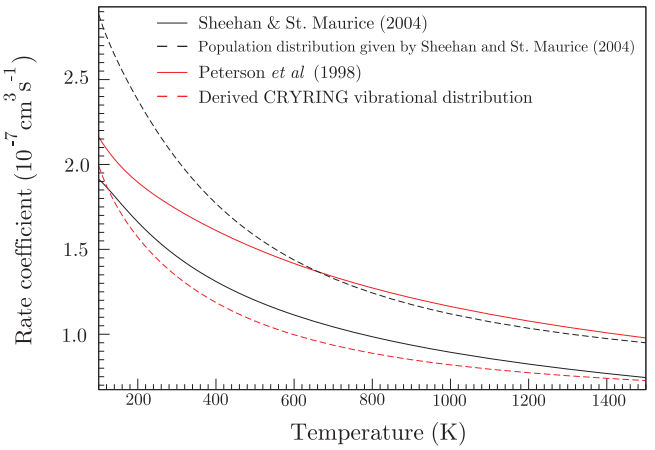

FIG. 16. (Color online) Comparison of our calculated, isotropic rate coefficients for N_2^+ DR with the measurements of Peterson *et al.* [7], and Sheehan and St. Maurice [8]. The experimental rate coefficients were recalculated using the cross sections from each respective study.

the ions are not vibrationally cool (Peterson *et al.* and Sheehan and St. Maurice) are both lower than those of $v_i^+ = 0$.

To compare our computed rate coefficient with the measurements of Peterson *et al.* and Sheehan and St. Maurice we have found rate coefficients using the cross sections they provided. Although rates of the form $A(T_e/T)^{-a}$ are provided in both studies, fittings of this form ignore a lot of structure due to the simple single-exponent temperature dependence. Sheehan and St. Maurice also recalculated an isotropic rate coefficient using the cross section of Peterson *et al.* and found a fitted value of $(1.50 \pm 0.23) \times 10^{-7}(T_e/300)^{-0.39}$ cm^{3}s^{-1} which has nearly perfect agreement with the value found for their merged beams experiment, $(1.50 \pm 0.23) \times 10^{-7}(T_e/300)^{-0.38}$ cm^{3}s^{-1}. The value we found at 300 K is 1.734×10^{-7} cm^{3}s^{-1}, which is similar to the original value given by Peterson *et al.*, $(1.75 \pm 0.09) \times 10^{-7}$ cm^{3}s^{-1}.

Figure 16 gives a comparison of our work scaled by the derived CRYRING and Sheehan and St. Maurice distributions with the rate coefficients calculated using their respective cross sections. Again we see that the Sheehan and St. Maurice vibrational distribution gives better agreement with the CRYRING results indicating that this may be closer to the true distribution. All of the rates have a very similar temperature dependence above 600 K; the vibrationally resolved rate coefficients in Fig. 17 also indicate that there is not a drastic change in temperature dependence with vibrational excitation. The divergence between the Sheehan and St. Maurice distribution and the CRYRING rate is due to resonance A (see Fig. 14) being slightly too low in energy and narrower than that measured in the CRYRING cross section.

Comparisons with available calculated rates from Guberman are presented in Fig. 17. The formula given by Guberman is $2.2^{+0.2}_{-0.4} \times 10^{-7}(T_e/300)^{-0.40}$ cm^{3}s^{-1}. When comparing unfitted and fitted, it is clear that fitting over a large temperature range (100–3000 K) averages out a lot of the structure. There is, however, good agreement between his and our $v_i^+ = 0$ rate fitted and unfitted. The rates for $v_i^+ = 1,2$ are very different in terms of both magnitude and temperature dependence.

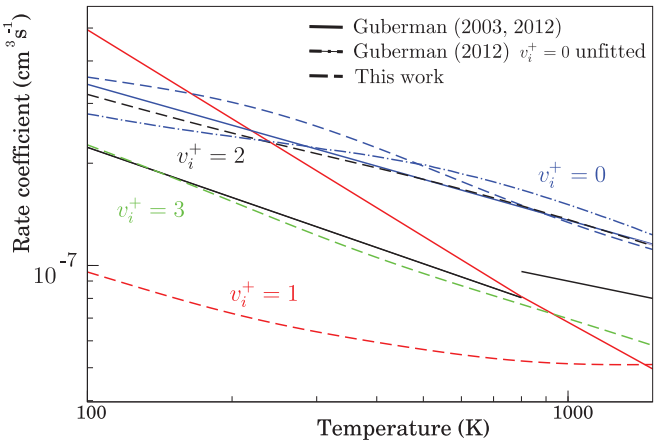

FIG. 17. (Color online) Comparison with Guberman's [15,17] isotropic N_2^+ DR rate coefficients. Guberman's fitted and unfitted values for $v_i^+ = 0$ are displayed for comparison.

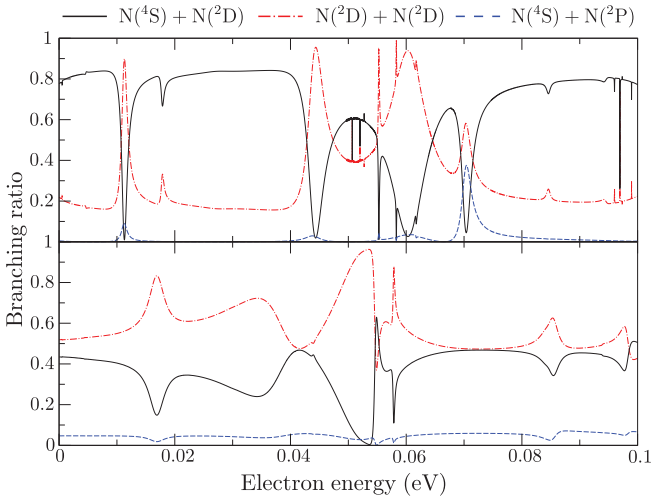

FIG. 18. (Color online) Energy-dependent branching ratios for $v_i^+ = 0$ (upper panel) and $v_i^+ = 1$ (lower panel).

3. *Summary of vibrational distribution discussion*

Overall the agreement between both experiments and experiment and theory is good. The agreement between our rate and Guberman's for $v_i^+ = 0$ is also good. It is, however, difficult to make a solid conclusion as to the actual vibrational population of each experiment. More weight should be placed on the vibrational distribution of Peterson *et al.* as this measurement took place on the ion beam used in the cross-section measurement. However, this measurement was taken at 0 eV relative collision energy and it is not guaranteed that the vibrational distribution will not change during the experiment. The fact that the $v_i^+ = 1$ DR cross section is much lower relative to the other vibrational level results in this vibrational state dominating the population. The better agreement with the vibrational distribution of Sheehan and St. Maurice indicates that this may be closer to the vibrational distribution in the CRYRING experiment.

D. Branching ratios

Branching ratios are calculated by simply summing the cross sections for each individual dissociative channel to each asymptote and dividing by the total cross section. A Landau-Zener calculation [42] was performed on the avoided crossing highlighted by the red box in Fig. 4; the crossing probability to the lower state was found to be 0.85 for $v_i^+ = 0$ and 0.87 for $v_i^+ = 1$. Therefore, 15% and 13% of the branching ratio going to N(^4S) + N(^2D) was subtracted and added to the branching ratio for N(^2D) + N(^2D) for $v_i^+ = 0$ and $v_i^+ = 1$, respectively. The branching ratios for $v_i^+ = 0,1$ are displayed in Fig. 18 for 10^{-5}–0.1 eV.

The branching ratios of the DR of N_2^+ were measured by Peterson *et al.* [7] for $v_i^+ = 0$ and its isotoplogue $^{15}N^{14}N^+$ by Kella *et al.* [39] for $v_i^+ = 0,1$ at zero relative energy. The use of $^{15}N^{14}N^+$ by Kella *et al.* meant that radiative rovibrational relaxation was possible due to the dipole of the molecule and the branching ratios for $v_i^+ = 0$ could be measured. Given the small difference between the ground vibrational state of $^{14}N_2^+$ and $^{15}N^{14}N^+$, a comparison between the measured rate of the isotoplogue and the calculated rate of the homonuclear $^{14}N_2^+$ is justified. Table II gives the branching ratio at 10^{-5} eV with a comparison with experimental data.

For $v_i^+ = 0$, agreement is reasonable if we consider that both experimental studies report that the majority of the cross section should go to N(^4S) + N(^2D) and N(^2D) + N(^2P). In our model there is no path to the N(^2D) + N(^2P) asymptote available at this energy which is confirmed by experiment. There is, however, a disparity between the experiment and the relative branching to these two products. The reasons for this are unclear; both this theoretical study and that of Guberman [17] suggest that the $2\,^3\Pi_u$ is the dominant state for $v_i^+ = 0$ which dissociates to N(^4S) + N(^2D). In Guberman's first study of the DR N_2^+ [14] he also calculates the crossing probability of the avoided crossing highlighted in Fig. 1 and finds a similar crossing probability of 0.88; this again is not enough to account for the difference between the theory and experiment. Kella *et al.* report that Guberman has recalculated branching ratios to be 0.70, 0.27, and 0.3 for N(^4S) + N(^2D), N(^2D) + N(^2D), and N(^4S) + N(^2P), respectively. To our knowledge, this calculation has not been reported in detail, but gives good agreement with our results.

TABLE II. Branching ratios, calculated and experimentally measured for $v_i^+ = 0,1$.

	Product channel	Branching ratio		
$v_i^+ = 0$		This work	Kella *et al.*	Peterson *et al.*
	N(^4S) + N(^2D)	0.776	0.46 ± 0.08	0.37 ± 0.08
	N(^4S) + N(^2P)	0.005	0.08 ± 0.06	0.11 ± 0.06
	N(^2D) + N(^2D)	0.219	0.46 ± 0.08	0.52 ± 0.04
	N(^2D) + N(^2P)	0.0	0.0	
$v_i^+ = 1$		This work	Kella *et al.*	
	N(^4S) + N(^2D)	0.434		
	N(^4S) + N(^2P)	0.047		
	N(^2D) + N(^2D)	0.519	0.5 ± 0.1	
	N(^2D) + N(^2P)	0.0	0.5 ± 0.1	

Due to the resolution of their experimental equipment Kella *et al.* were only able to measure the branching ratios for the $N(^2D) + N(^2D)$ and $N(^2D) + N(^2P)$ asymptotes which they found to be equal. In our model only 1% of the cross section is going to the $N(^2D) + N(^2P)$ asymptote and just under half to $N(^2D) + N(^2D)$. The branching ratios for $v_i^+ = 1$ are very similar to the measured values for $v_i^+ = 0$.

Figure 1 shows the many avoided crossings in the superexcited states of N_2, some strongly avoided. It may be that accounting for these avoided crossings in a more rigorous way is key to reproducing the experimental results. A time-dependent wave-packet calculation [43] would provide more information about the final-state products. The relevant input information to perform this calculation is available in the Supplemental Material [44].

VI. CONCLUSION

The calculated cross section has excellent agreement with experiment and also reproduces the two main structures in the CRYRING [7] cross section. The cross section is completely *ab initio*; no empirical data has been introduced into the calcuation at any point. This shows that the *R*-matrix method coupled with the MQDT approach presented in this paper provides a self-consistent and accurate *ab initio* approach to calculating DR cross sections. As with previous theoretical studies by Guberman [14–18] this study shows that the most important symmetry for the DR of N_2^+ is $^3\Pi_u$. The main difference between the model presented here and that of Guberman is the relative importance of the 2 $^3\Pi_u$ and 4 $^3\Pi_u$ states. It is interesting to note that, although the potential-energy curve crossing positions were similar in both studies, the couplings were not. Nevertheless, both results, at least for $v_i^+ = 0$, resulted in good agreement with experiment. There is strong experimental evidence to suggest that the $v_i^+ = 1$ rate is lower than the $v_i^+ = 0$ one; this study also suggests that this is the case. The vibrationally resolved rates we have calculated indicate that there is not a strong vibrational dependence on temperature dependence; this is in agreement with previous studies [7,8].

The branching ratios still remain uncertain from a theoretical point of view; taking into account the many avoided crossings present in the original adiabatic potential energy curves or the use of the time-dependent wave-packet method may shed more light on this issue.

ACKNOWLEDGMENTS

We thank Themisys Limited for supporting a studentship for D.A.L. D.A.L. would also like to thank A. Al-Refaie and C. Sousa-Silva for their help and support. I.F.S. acknowledges support from the International Atomic Energy Agency via the Coordinated Research Project "Light Element Atom, Molecule and Radical Behaviour in the Divertor and Edge Plasma Regions," from Agence Nationale de la Recherche via the projects "SUMOSTAI" (No. ANR-09-BLAN-020901) and "HYDRIDES" (No. ANR-12-BS05-0011-01), from the IFRAF-Triangle de la Physique via the project "SpecoRyd," and from the Centre National de la Recherche Scientifique via the programs "Physique et Chimie du Milieu Interstellaire," and the PEPS projects "Physique théorique et ses interfaces" TheMS and TPCECAM. He also acknowledges generous financial support from La Région Haute-Normandie via the CPER "THETE" project, and the GRR Electronique, Energie et Matriaux, from the "Fédération de Recherche Energie, Propulsion, Environnement," and from the LabEx EMC^3, via the project PicoLIBS (No. ANR-10-LABX-09-01). He also thanks the Laboratoire Aimé Cotton for hospitality. K.C. thanks the department Institut des Sciences de l'Ingénierie et des Systèmes (INSIS) of CNRS for a research grant in 2013, and Laboratoire Ondes et Milieux Complexes (LOMC) of Le Havre University for hospitality.

[1] A. Bultel and J. Annaloro, Plasma Sources Sci. Technol. **22**, 025008 (2013).
[2] O. Dutuit, N. Carrasco, R. Thissen, V. Vuitton, C. Alcaraz, P. Pernot, N. Balucani, P. Casavecchia, A. Canosa, S. Le Picard *et al.*, Astrophys. J. Suppl. **204**, 20 (2013).
[3] M. Capitelli, G. Colonna, G. D'Ammando, V. Laporta, and A. Laricchiuta, Chem. Phys. **438**, 31 (2014).
[4] I. N. Kadochnikov, B. I. Loukhovitski, and A. M. Starik, Plasma Sources Sci. Technol. **22**, 035013 (2013).
[5] M. Larsson and A. E. Orel, *Dissociative Recombination of Molecular Ions*, Cambridge Molecular Science (Cambridge University Press, New York, UK, 2008).
[6] A. I. Florescu-Mitchell and J. B. A. Mitchell, Phys. Rep. **430**, 277 (2006).
[7] J. R. Peterson, A. Le Padellec, H. Danared, G. H. Dunn, M. Larsson, A. Larson, R. Peverall, C. Stromholm, S. Rosen, M. af Ugglas *et al.*, J. Chem. Phys. **108**, 1978 (1998).
[8] C. H. Sheehan and J.-P. St.-Maurice, J. Geophys. Res.: Space Phys. **109**, A03302 (2004).
[9] A. J. Cunningham and R. M. Hobson, J. Phys. B: At. Mol. Opt. Phys. **5**, 2328 (1972).
[10] E. C. Zipf, Geophys. Res. Lett. **7**, 645 (1980).
[11] M. R. Mahdavi, J. B. Hasted, and M. M. Nakshbandi, J. Phys. B: At. Mol. Opt. Phys. **4**, 1726 (1971).
[12] M. Geoghegan, N. G. Adams, and D. Smith, J. Phys. B: At. Mol. Opt. Phys. **24**, 2589 (1991).
[13] A. Canosa, J. C. Gomet, B. R. Rowe, and J. L. Queffelec, J. Chem. Phys. **94**, 7159 (1991).
[14] S. L. Guberman, Geophys. Res. Lett. **18**, 1051 (1991).
[15] S. Guberman, *Dissocative Recombination of Molecular Ions with Electrons* (Kluwer/Plenum Publishers, New York, 2003), pp. 187–196.
[16] S. L. Guberman, J. Phys. Chem. A **111**, 11254 (2007).
[17] S. L. Guberman, J. Chem. Phys. **137**, 074309 (2012).
[18] S. L. Guberman, J. Chem. Phys. **139**, 124318 (2013).

[19] D. A. Little and J. Tennyson, J. Phys. B: At. Mol. Opt. Phys. **46**, 145102 (2013).
[20] D. A. Little and J. Tennyson, J. Phys. B: At. Mol. Opt. Phys. **47**, 105204 (2014).
[21] J. Tennyson, Phys. Rep. **491**, 29 (2010).
[22] B. K. Sarpal, J. Tennyson, and L. A. Morgan, J. Phys. B: At. Mol. Opt. Phys. **27**, 5943 (1994).
[23] I. F. Schneider, I. Rabadán, L. Carata, J. Tennyson, L. H. Andersen, and A. Suzor-Weiner, J. Phys. B: At. Mol. Opt. Phys. **33**, 4849 (2000).
[24] O. Motapon, M. Fifirig, A. Florescu, F. O. Waffeu-Tamo, O. Crumeyrolle, G. Varin-Breant, A. Bultel, P. Vervisch, J. Tennyson, and I. F. Schneider, Plasma Sources Sci. Technol. **15**, 23 (2006).
[25] J. M. Carr, P. G. Galiatsatos, J. D. Gorfinkiel, A. G. Harvey, M. A. Lysaght, D. Madden, Z. Masin, M. Plummer, and J. Tennyson, Eur. Phys. J. D **66**, 58 (2012).
[26] I. Rabadán and J. Tennyson, J. Phys. B: At. Mol. Opt. Phys. **29**, 3747 (1996).
[27] D. A. Little *et al.*, Comput. Phys. Comms. (to be published).
[28] D. T. Stibbe and J. Tennyson, Comput. Phys. Commun. **114**, 236 (1998).
[29] J. Tennyson, J. Phys. B: At. Mol. Opt. Phys. **29**, 1817 (1996).
[30] F. T. Smith, Phys. Rev. **118**, 349 (1960).
[31] D. T. Stibbe and J. Tennyson, J. Phys. B: At. Mol. Opt. Phys. **29**, 4267 (1996).
[32] J. B. Roos, A. E. Orel, and A. Larson, Phys. Rev. A **79**, 062510 (2009).
[33] L. Carata, A. E. Orel, M. Raoult, I. F. Schneider, and A. Suzor-Weiner, Phys. Rev. A **62**, 052711 (2000).
[34] I. F. Schneider, O. Dulieu, A. Giusti-Suzor, and E. Roueff, Astrophys. J. **424**, 983 (1994).
[35] A. Giusti, J. Phys. B: At. Mol. Opt. Phys. **13**, 3867 (1980).
[36] V. Ngassam, A. Florescu, L. Pichl, I. Schneider, O. Motapon, and A. Suzor-Weiner, Eur. Phys. J. D **26**, 165 (2003).
[37] M. J. Seaton, Rep. Prog. Phys. **46**, 167 (1983).
[38] K. Chakrabarti, D. R. Backodissa-Kiminou, N. Pop, J. Z. Mezei, O. Motapon, F. Lique, O. Dulieu, A. Wolf, and I. F. Schneider, Phys. Rev. A **87**, 022702 (2013).
[39] D. Kella, P. J. Johnson, H. B. Pedersen, L. Vejby-Christensen, and L. H. Andersen, Phys. Rev. Lett. **77**, 2432 (1996).
[40] C. Noren, F. B. Yousif, and J. B. A. Mitchell, J. Chem. Soc., Faraday Trans. 2 **85**, 1697 (1989).
[41] H. Kreckel, A. Petrignani, O. Novotny, K. Crabtree, H. Buhr, B. J. McCall, and A. Wolf, Philos. Trans. R. Soc. A **370**, 5088 (2012).
[42] D. Marx and J. Hutter, *Ab Initio Molecular Dynamics Basic Theory and Advanced Methods* (Cambridge University Press, New York, UK, 2009).
[43] A. E. Orel, J. Phys. Conf. Ser. **4**, 142 (2005).
[44] See Supplemental Material at http://link.aps.org/supplemental/10.1103/PhysRevA.90.052705 for [brief description].